Applied Physics A (2019) 125:375
https://doi.org/10.1007/s00339-019-2665-y

Applied Physics A
Materials Science & Processing

Effect of titanium substitution on the structural, magnetic and magnetocaloric properties of $La_{0.67}Ba_{0.25}Ca_{0.08}MnO_3$ perovskite manganites

Marwa Bourguiba[1,2] · Mohamed Amara Gdaiem[3] · Moez Chafra[1] · E. K. Hlil[4] · Hafedh Belmabrouk[5] · Abdullah Bajahzar[6]

Received: 4 March 2019 / Accepted: 24 April 2019 / Published online: 2 May 2019

Abstract

We have studied the effect of Mn substitution by Ti on the structural, magnetic and magnetocaloric properties of $La_{0.67}Ba_{0.25}Ca_{0.08}MnTiO_3$ samples. All samples were synthesized using the flux method. X-ray powder diffraction showed that our samples crystallize in the rhombohedral phase $R\bar{3}c$ space group. According to the magnetic properties, our samples present a transition from a paramagnetic to a ferromagnetic phase upon decreasing temperature. The deviation of the inverse curve of the magnetic susceptibility from Curie–Weiss law indicates the existence of a Griffiths phase. This reveals the presence of ferromagnetic clusters in paramagnetic region. Regarding the positive slopes of Arrott's plots, the universal theory and the Landau $B(T)$ coefficient value sign demonstrate the second-order magnetic phase transition. The magnetic entropy change was determined based to Maxwell's relations and Landau's theory. Near room temperature, our samples exhibited an important magnetic entropy change with maxima of 3.21 and 2.76 J kg^{-1} K^{-1}, under an applied magnetic field of 5 T, respectively, for $La_{0.67}Ba_{0.25}Ca_{0.08}MnO_3$ and $La_{0.67}Ba_{0.25}Ca_{0.08}Mn_{0.95}Ti_{0.05}O_3$. Relative cooling power was estimated as well. It was found to reach 168 and 187 J/kg for $La_{0.67}Ba_{0.25}Ca_{0.08}MnO_3$ and $La_{0.67}Ba_{0.25}Ca_{0.08}Mn_{0.95}Ti_{0.05}O_3$, respectively. From the hysteresis cycles, our studied sample showed a typical soft ferromagnetic behavior with a low coercive field at 10 K. These results make our samples promising candidates for magnetic refrigeration.

1 Introduction

Perovskite manganese oxides with the general formula $Re_{1-x}A_xMnO_3$ (Re = rare-earth and A = divalent alkaline earth ions) have been revitalized in the last few years, this interest is due to their attractive electrical and magnetic properties [1–5] and their importance for several applications, such as in spintronics, information storage, magnetic recording media, gas sensors and magnetic refrigeration applications [6–8]. In addition, these materials have many advantages, such as their low production cost, convenient preparation, high refrigeration efficiency, small volume requirement and chemical stability. Besides, these materials are environment-friendly, non toxic and do not cause for noise pollution. This makes them attractive to further research in relation to the widely used refrigeration technology based on gas compression. To understand the different physical properties of these materials, many theories such as double-exchange (DE) interaction and Griffiths singularity have been proposed [9]. Basically, these physical phenomena are directly related to ferromagnetic (FM) or antiferromagnetic (AFM) interactions. According to DE

✉ Mohamed Amara Gdaiem
gdaiem_mohamed@hotmail.fr

[1] Laboratoire de recherche en Mécanique Appliquée et systèmes (LASMAP-EPT), Ecole Polytechnique de Tunisie, Université de Carthage, La Marsa, Tunisia

[2] Faculté des sciences de Tunis, Université de Tunis el Manar, 2092 Tunis, Tunisia

[3] Laboratoire de la Matière Condensée et des Nanosciences, Département de Physique, Faculté des Sciences de Monastir, 5019 Monastir, Tunisia

[4] Institut Neel, CNRS et Université Joseph Fourier, B, P, 166, 38042 Grenoble, France

[5] Department of Physics, College of Science at Zulfi, Majmaah University, Zulfi 11932, Saudi Arabia

[6] Department of Computer Science and Information, College of Science at Zulfi, Majmaah University, Zulfi 11932, Saudi Arabia

phenomenon, the charge carrier of the system, for example, transfers from Mn^{3+} to Mn^{4+} via oxygen. Furthermore, the strong Hund's coupling between the Mn site and for example, causes an FM interaction, while Mn^{3+}–O^{2-}–Mn^{3+} and Mn^{4+}–O^{2-}–Mn^{4+} super exchange (SE) interaction makes an AFM ordering. Consequently, according to the ratio of Mn^{3+}/Mn^{4+} ions, these two orders can coexist in a single sample. However, DE phenomenon is insufficient to explain the importance of physical properties in manganites. In addition, Griffiths phase can explain these complex phenomena. Recently, Griffiths phase has been used to survey the magnetic properties of diverse compounds, such as: rare-earth inter-metallic compounds $Tb_5Si_2Ge_2$ [10] and hole perovskite-doped manganites [11–15]. The existence of Griffiths phase is due to the presence of FM clusters in paramagnetic (PM) parts. Besides, the physical properties of perovskite managnites are highly influenced by other factors, such as the method of preparation and the doping level in the Re (La) or Mn site. For instance, doping $LaMnO_3$ sample in the La site by Sr^{2+} involves the presence of the mixed valence Mn^{3+} and Mn^{4+} at the Mn site, and this compound ($LaSrMnO_3$) becomes FM and conducting. These manganites are acquiring a growing interest in magnetic refrigeration technology for their large magnetocaloric effect (MCE) [16]. In addition, $La_{0.67}Ca_{0.33}MnO_3$ presents a second-order transition at 272 K and a large MCE ($-\Delta S_M = 3.6$ J/kg K) under an applied magnetic field of 1 T [17]. Betancourt et al. have been reported that $La_{0.67}Ba_{0.33}MnO_3$ sample shows a $-\Delta S_M$ of 1.06 J/kg K under an applied magnetic field of 2.5 T at 340 K, which makes this sample a potential candidate for magnetic refrigeration [18]. The sample $La_{0.67}Ba_{0.22}Sr_{0.11}MnO_3$ presents large $-\Delta S_M$ of about 2.26 J/kg K at $\mu_0 H = 5T$ and a Curie temperature (T_C) at 450 K [19], while the value of $-\Delta S_M = 4.91$ J/kg K at $T_C = 350$ K and $\mu_0 H = 5T$ for $La_{0.67}Ba_{0.23}Ca_{0.1}MnO_3$ composition [20]. However, its T_C is remote from room temperature, restricting its applicability in traditional cooling devices.

To adjust these physical properties, Mn-site itself is doped with other transition elements such as In, Cr, Co, Fe, Ti, Al [19, 21–24]. Recently, it has been shown that with increasing the doping rate of Fe at B-site, T_C and $-\Delta S_M$ decrease [25]. Reshmi et al. state that the Ni substitution in $La_{0.67}Sr_{0.33}MnO_3$ reduced T_C to about room temperature but the maximum of $-\Delta S_M$ decreased.

This paper aims at studying the effect of titanium on the structural, magnetic and MCE properties in $La_{0.67}Ba_{0.25}Ca_{0.08}MnO_3$ compound.

2 Experimental details

The flux method is a simple and low-cost strategy to prepare materials. It cannot affect the microstructure [26, 27]. In this process, for $La_{0.67}Ba_{0.25}Ca_{0.08}MnO_3$ sample, stoichiometric amounts of La_2O_3, $BaCO_3$, $CaCO_3$ and MnO_2 precursors were taken in the appropriate molar ratio. For $La_{0.67}Ba_{0.25}Ca_{0.08}Mn_{0.95}Ti_{0.05}O_3$ sample, La_2O_3, $BaCO_3$, $CaCO_3$, MnO_2 and TiO_2 precursors were used. The mixture was ground in an agate mortar for 2 h with an appropriate quantity of KCl. The adding of KCl is to expedite thermal ionic diffusion in the solid state, thereby weakening the activation barriers to ceramic synthesis and sintering. In addition, it avoids the evaporation of precursors. The obtained powder was heated in an alumina crucible at 800 °C for 24 h. Then, it was washed with hot distilled water to remove KCl salts. The residue was dried at 100 °C in air. After being ground well, the powders were pressed at 10^5 Pa into circular pellets ($e = 1$ mm and $d = 10$ mm), then sintered in the air at 1000 °C for 24 h. The structure and phase purity of the prepared samples were verified by X-ray diffraction (XRD), using the "PANalytical X'Pert Pro" diffractometer with a Cukα radiation ($\lambda = 1.5406$ Å) at room temperature. Data refinement was obtained with 2θ from 10° to 70°, with a scanning step of 0.02° and a counting time of 18 s per step. The structural analysis was carried out by the standard Rietveld Method [28], using the program FULLPROF [29]. The microstructure was studied by scanning electron microscopy (SEM) on the as-obtained pellets using a 'Phillips XL 30 microscope'. A semi-quantitative analysis was done at 20 kV accelerating voltage using energy dispersive X-ray analyses (EDX). The dc magnetic properties were carried out over a temperature range of 0–400 K in an applied magnetic field of 0.05 T in both zero-field cooled (ZFC) and field-cooled (FC) modes. These experiments were carried out using a BS2 and BS1 magnetometer developed in Louis Neel Laboratory of Grenoble.

3 Results and discussion

3.1 Structural analysis

To study the structural properties of our samples, we carried out XRD analysis with CuKα radiation at room temperature. XRD diagrams of our samples are presented in Fig. 1. We can remark that our samples have a single phase without any detectable secondary phase, within the sensitivity limits of the experimental. Zooming the most intense peak, we can also remark a shift of peak to lower 2θ values (inset of Fig. 1).This explains the increase of the unit cell volume with increasing Ti content [30]. This confirms the incorporation of Ti (equal to 0.605 Å) at the Mn site and the ratio c/a exhibits the anisotropic contractions [31, 32]. The structural refinement indicates the rhombohedral structure with the space group $R\bar{3}c$ (no. 167), in which La/Ba/Ca atoms at 6a (0, 0, 1/4) position, Mn/Ti at 6b (0, 0, 0) and O at 18e (x, 0, 1/4) position. The Rietveld analysis,

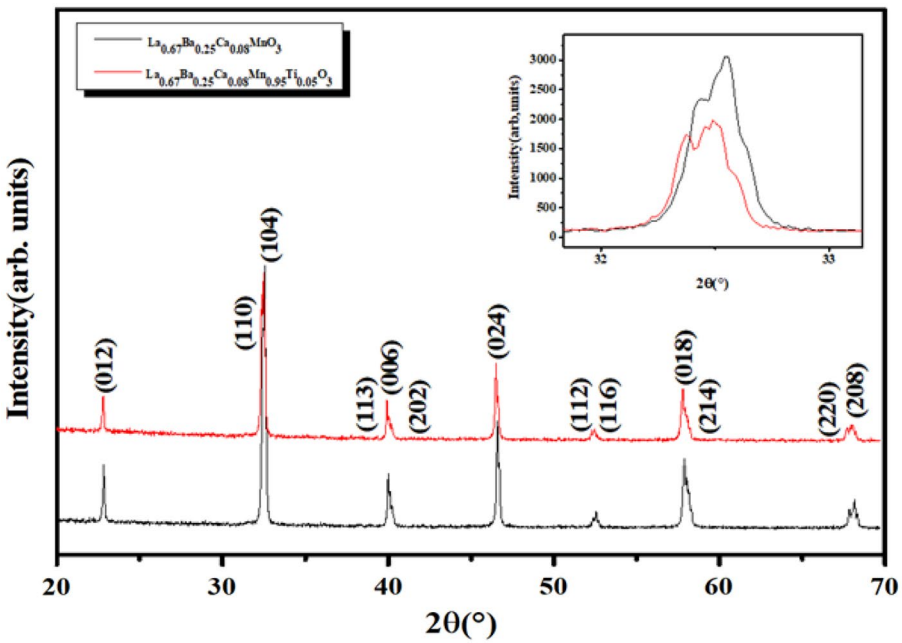

Fig. 1 XRD patterns for $La_{0.67}Ba_{0.25}Ca_{0.08}MnO_3$ and $La_{0.67}Ba_{0.25}Ca_{0.08}Mn_{0.95}Ti_{0.05}O_3$ samples. The inset shows the most intense peak of our samples (Bragg reflexions 104)

is depicted in Fig. 2a, a* for $La_{0.67}Ba_{0.25}Ca_{0.08}MnO_3$ and $La_{0.67}Ba_{0.25}Ca_{0.08}Mn_{0.95}Ti_{0.05}O_3$, respectively. The quality of XRD data refinement is estimated by the adjustment indicator such as the weighted pattern R_{wp}, pattern R_p, and the goodness of fit χ^2. A good agreement between the experimental and calculated XRD pattern is shown. The obtained results are summarized in Table 1. The increase of unit cell volume with increasing Ti is accompanied by an increase of d_{Mn-O} length and a decrease of $\theta_{Mn-O-Mn}$ bond angle of MnO_6 (Table 1). The crystal structure and the distances Mn–O for $La_{0.67}Ba_{0.25}Ca_{0.08}Mn_{0.95}Ti_{0.05}O_3$ sample were determined using "Diamond" program, based on the evaluated atomic positions. As shown in the inset (b*) of Fig. 2a*.

To predict the stability of perovskite structure, Goldschmidt proposed a tolerance factor (t), defined as [33]:

$$t = \frac{< r_A > + < r_O >}{\sqrt{2}(< r_B > + < r_O >)}, \quad (1)$$

where $\langle r_A \rangle$, $\langle r_B \rangle$ and $\langle r_O \rangle$ are the average ionic radii of A, B and O perovskite sites, respectively. Generally, we can say that any sample has a perovskite structure if its t lies in the limits of $0.89 < t < 1.02$ [34]. In our work, the values of t were found to be 0.942 and 0.941 for $La_{0.67}Ba_{0.25}Ca_{0.08}MnO_3$ and $La_{0.67}Ba_{0.25}Ca_{0.08}Mn_{0.95}Ti_{0.05}O_3$, respectively. Hence, our samples are in the stable range of perovskite structure.

From the reflection of 2θ values of XRD profile, the average crystallite size (D_{sc}) was calculated using Scherer's equation. It is defined as [35]:

$$D_{sc} = \frac{K\lambda}{\beta \cos\theta}, \quad (2)$$

where λ is the wavelength of the CuKα radiation ($\lambda = 1.5406$ Å), K is a form factor of value 0.9, θ is the position of the peak in degrees and β is the width at mid-height of the most intense peak.

The obtained values of D_{sc} decrease from 34 to 30 nm, respectively, for $La_{0.67}Ba_{0.25}Ca_{0.08}Mn_{0.95}Ti_{0.05}O_3$ and $La_{0.67}Ba_{0.25}Ca_{0.08}MnO_3$. This proves the nano-metric size of our samples [36].

Another method can be used to calculate the average crystallite size, based on the analysis of all diffraction peaks. It is Williamson–Hall's approach (WH), defined as [37]:

$$\beta \cos\theta = \frac{K\lambda}{D_{WH}} + 4\varepsilon \sin\theta. \quad (3)$$

The plot of $\beta\cos\theta$ versus 4 $\sin\theta$ is presented in inset (c) and (c*) of Fig. 2, $La_{0.67}Ba_{0.25}Ca_{0.08}MnO_3$ and $La_{0.67}Ba_{0.25}Ca_{0.08}Mn_{0.95}Ti_{0.05}O_3$, respectively. The micro strain (ε) is extracted from the inverse of the slope of the linearly fitted data, and D_{WH} is calculated from the root of the y intercept.

The values of D_{WH} were equal to 137 and 99 nm, for $La_{0.67}Ba_{0.25}Ca_{0.08}MnO_3$ and $La_{0.67}Ba_{0.25}Ca_{0.08}Mn_{0.95}Ti_{0.05}O_3$, respectively. We can see that these values are larger than D_{sc}. This difference is caused by the existence of strain, which contributes to the broadening of peaks [38]. The surface morphology of our samples was interpreted with SEM image as shown in the insets (b) and (b*) of Fig. 3a, a*, for $La_{0.67}Ba_{0.25}Ca_{0.08}MnO_3$ and $La_{0.67}Ba_{0.25}Ca_{0.08}Mn_{0.95}Ti_{0.05}O_3$. The average particle sizes of the compounds were estimated using Image J software. After measuring the diameters of all the particles in SEM image, the obtained data were fitted with the log–normal function [39]:

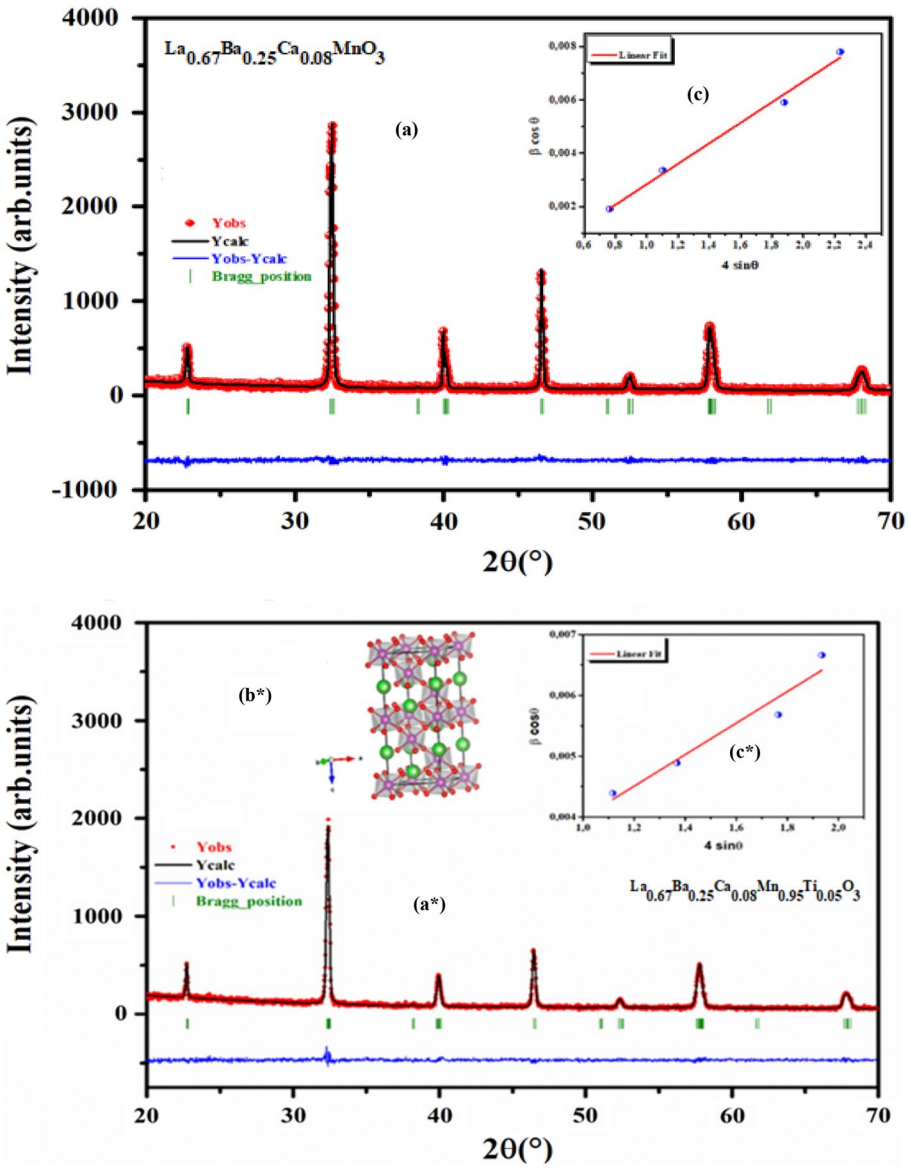

Fig. 2 (a) and (a*) show Rietveld plots of XRD data for $La_{0.67}Ba_{0.25}Ca_{0.08}MnO_3$ and $La_{0.67}Ba_{0.25}Ca_{0.08}Mn_{0.95}Ti_{0.05}O_3$ samples, respectively. The inset (b*) shows the crystal structure, for $La_{0.67}Ba_{0.25}Ca_{0.08}Mn_{0.95}Ti_{0.05}O_3$ as an example. The inset (c) and (c*) show Williamson–Hall graph of our samples

$$f(D) = \left(\frac{1}{\sqrt{2\pi}\sigma D}\right) \exp\left[-\frac{\ln^2\left(\frac{D}{D_0}\right)}{2\sigma^2}\right], \quad (4)$$

where D_0 and σ are the median diameter obtained from the SEM and data dispersions, respectively. The insets (c) and (c*) of Fig. 3a, a*, for $La_{0.67}Ba_{0.25}Ca_{0.08}MnO_3$ and $La_{0.67}Ba_{0.25}Ca_{0.08}Mn_{0.95}Ti_{0.05}O_3$, respectively, show the dispersion histogram. The mean diameter $\langle D\rangle = D_0 \exp(\sigma^2/2)$ and standard deviation $\sigma_D = \langle D\rangle\,[\exp(\sigma^2) - 1]^{1/2}$ were determined using fit results. The grain sizes observed by SEM were equal to 1.89 and 1.29 µm, for $La_{0.67}Ba_{0.25}Ca_{0.08}MnO_3$ and $La_{0.67}Ba_{0.25}Ca_{0.08}Mn_{0.95}Ti_{0.05}O_3$, respectively. These are larger than those calculated by Scherer and Williams–Hall methods. This is because each particle observed by SEM consists of several crystallized grains [40, 41].

To verify the existence of all elements in our studied sample, energy-dispersive X-ray analysis (EDX) was carried out at room temperature. EDX spectrum depicted in Fig. 3a, a*, for $La_{0.67}Ba_{0.25}Ca_{0.08}MnO_3$ and $La_{0.67}Ba_{0.25}Ca_{0.08}Mn_{0.95}Ti_{0.05}O_3$, respectively, shows the presence of all elements. This confirms that there is no loss of any integrated elements during the sintering with in experimental errors. The typical cationic composition for our samples is listed in Table 2. This confirms the absence of secondary phases in the X-rays and the cationic composition of our samples.

Table 1 Structural parameters of $La_{0.67}Ba_{0.25}Ca_{0.08}MnO_3$ and $La_{0.67}Ba_{0.25}Ca_{0.08}Mn_{0.95}Ti_{0.05}O_3$ samples deduced from Rietveld refinement of XRD data at room temperature

Compositions	$La_{0.67}Ba_{0.25}Ca_{0.08}MnO_3$	$La_{0.67}Ba_{0.25}Ca_{0.08}Mn_{0.95}Ti_{0.05}O_3$
Cell parameters		
a (Å)	5.530 (7)	5.521 (1)
c (Å)	13.453 (8)	13.557 (3)
V (Å^3)	356.39 (8)	357.894 (5)
Atoms		
(La/Ba/Ca) (6a) Biso (A$^{\circ 2}$)	0.537	0.199
(Mn/Ti) (6b) Biso (A$^{\circ 2}$)	0.154	0.155
x (O)	0.468 (7)	0.454 (5)
Bond lengths and bond angles		
d_{Mn-O} (A$^{\circ}$)	1.957	1.970
$\theta_{Mn-O-Mn}$ (°)	169.64	165.20
W (u.a)$_{\times}(10^{-2})$	9.49	9.24
Agreement factors		
R_P (%)	9.54	10.7
R_{WP} (%)	12.2	13.6
χ^2	2.22	2.84

3.2 Magnetic properties

After careful study of the structural and morphological properties, we studied the magnetic properties of $La_{0.67}Ba_{0.25}Ca_{0.08}MnO_3$ and $La_{0.67}Ba_{0.25}Ca_{0.08}Mn_{0.95}Ti_{0.05}O_3$beginning with the zero-field-cooled (ZFC) and field-cooled (FC) magnetizations under an applied field of 0.05 T in the temperature range 0–400 K (Fig. 4). We can remark a net PM–FM transition, at their T_C. T_C, defined as the temperature corresponding to the peak of dM/dT in the M versus T curve, shown in inset of Fig. 4, are 300 and 287 K for $La_{0.67}Ba_{0.25}Ca_{0.08}MnO_3$ and $La_{0.67}Ba_{0.25}Ca_{0.08}Mn_{0.95}Ti_{0.05}O_3$, respectively. Additionally, a small divergence between ZFC and FC curves was noticed at the irreversibility temperature T = 264 and 258 K, respectively $La_{0.67}Ba_{0.25}Ca_{0.08}MnO_3$ and $La_{0.67}Ba_{0.25}Ca_{0.08}Mn_{0.95}Ti_{0.05}O_3$. This phenomenon can be attributed to the appearance of an isotropic field generated from FM clusters [42].

According to DE model, a lower T_C is associated to a poor overlap between Mn_{3d} and O_{2p} orbitals. This caused a reduction in the charge carrier bandwidth (W), which led to the decrease of the exchange coupling of Mn^{3+}–Mn^{4+} as well as T_C [43].

W can be expressed empirically by [44]:

$$W = \frac{\cos\omega}{d^{3.5}(\mathrm{Mn-O})}, \tag{5}$$

where ω is the plane "inclination" angle of the bond given by $\omega = (\pi - <\mathrm{Mn-O-Mn}>)/2$ and d_{Mn-O} is the bond length [43]. The calculated values of W are listed in Table 1. With substitution Mn^{4+} by Ti^{4+}, we can see that grain size decreases. This leads a decrease of $\theta_{Mn-O-Mn}$ angles. This caused a reduction in the charge carrier W, which led to the decrease of the exchange coupling of Mn^{3+}–Mn^{4+} as well as T_C.

To get insight into the magnetic behavior in FM phase, we determined M(T) curves on FC modes by the conventional spin wave theory. Generally, in correlated electron systems such as: manganite; spin waves, their fluctuations and domain boundaries are quite common in influencing the ferromagnetism [45]. According to Lonzarich and Taillefer, [46] the magnetization in any manganite sample is governed by the spin wave theory. Regarding this theory, magnetization varies as $T^{3/2}$ (Bloch's law), at low temperatures. Another term was added over a wide range of temperatures; it is T^2. While, close to T_C, it varies as $(1 - T^{4/3}/T_C^{4/3})^{1/2}$. Taking account of different parameters, in FM region, the magnetization data can be expressed by [46]:

$$M(T) = M_0 + M_{3/2}T^{3/2} + M_2T^2, \tag{6}$$

where M_0 is the temperature independent spontaneous magnetization. From the best fit curves in Fig. 4, we can conclude that FM behavior $La_{0.67}Ba_{0.25}Ca_{0.08}MnO_3$ and $La_{0.67}Ba_{0.25}Ca_{0.08}Mn_{0.95}Ti_{0.05}O_3$ samples may be due to spin waves.

To understand the dynamics of spin, we determined the susceptibility (χ^{-1}) as a function of temperature, as shown in Fig. 5. In PM region, all curves deviated from the linear behavior and showed a downturn in the curves, which is a characteristic of Griffiths phase [47, 48]. Griffith's law suggested that the deviation from the Curie–Weiss's law can be associated to the existence of FM clusters in PM region, signifying the presence of FM interaction.

The Griffiths temperature (T_G) is the maximum of the (d(χ^{-1})/dT) (T) curves [Inset (b) and (b*) of Fig. 6a, a*, for $La_{0.67}Ba_{0.25}Ca_{0.08}MnO_3$ and $La_{0.67}Ba_{0.25}Ca_{0.08}Mn_{0.95}Ti_{0.05}O_3$, respectively]. It is grouped in Table 3.

From Figs. 5 and 6, the $\chi^{-1}(T)$ curves present a nonlinear behavior, which indicates that the χ^{-1} (T) does not obey the Curie–Weiss's law. However, it must follow Curie–Weiss's law, in the region of $T > T_G$. This indicates a typical PM behavior, defined as [49]:

$$\chi = \frac{C}{T - \theta_{cw}}, \tag{7}$$

where θ_{cw} is Curie–Weiss temperature. C is the Curie constant, which present the inverse of the slope of the straight line. It is expressed by:

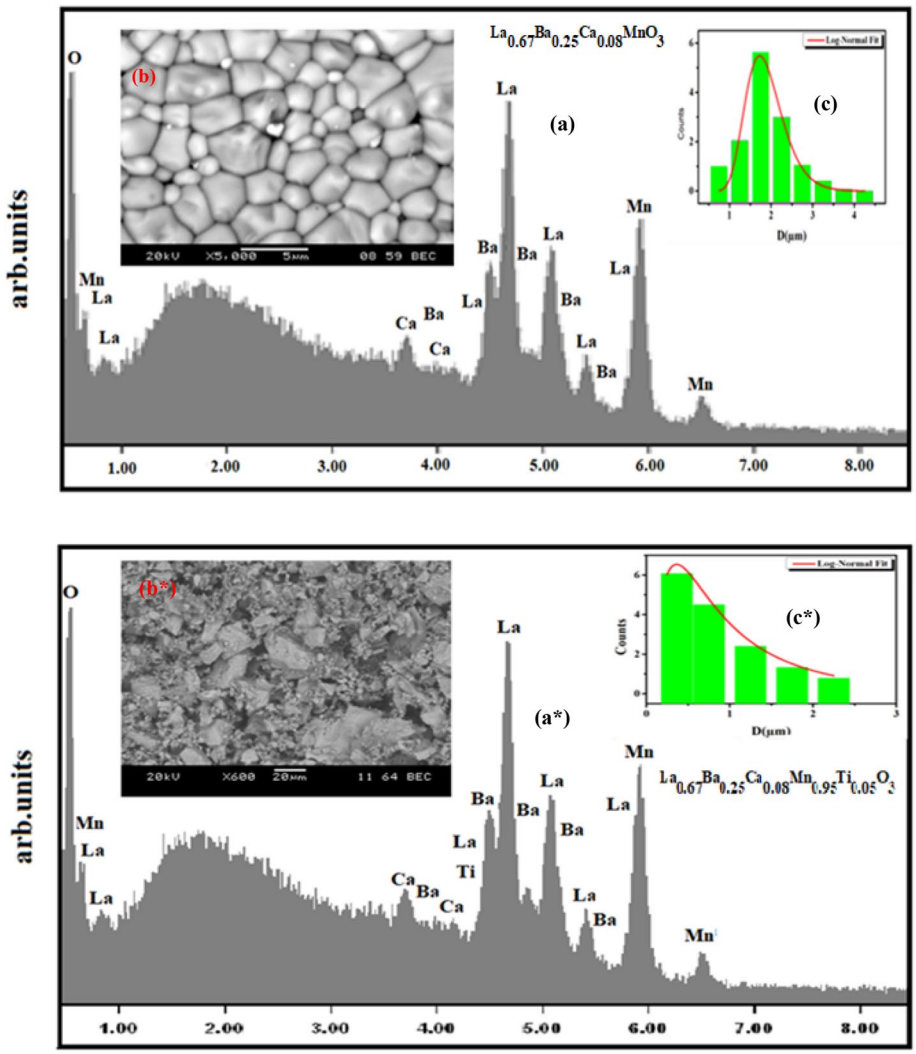

Fig. 3 (a) and (a*) show EDX analysis for $La_{0.67}Ba_{0.25}Ca_{0.08}MnO_3$ and $La_{0.67}Ba_{0.25}Ca_{0.08}Mn_{0.95}Ti_{0.05}O_3$ samples, respectively. Insets: (b) and (b*) show the typical SEM. The insets: (c) and (c*) show the histogram of the distribution of particle size

Table 2 Results of EDX analysis

Nominal composition	Typical cationic composition from EDX				
	La	Ba	Ca	Mn	Ti
$La_{0.67}Ba_{0.25}Ca_{0.08}MnO_3$	0.671	0.251	0.079	0.999	–
$La_{0.67}Ba_{0.25}Ca_{0.08}Mn_{0.95}Ti_{0.05}O_3$	0.670	0.251	0.08	0.952	0.049

$$C = \frac{N_A \mu_B^2}{3k_B} \mu_{\text{eff}}^{\text{exp}\,2}, \tag{8}$$

where $N_A = 6.023.10^{23}$ mol^{-1} is the Avogadro number; $\mu_B = 9.274.10^{-21}$ emu is the Bohr magneton and $k_B = 1.380\,16.10^{-16}$ erg k^{-1} is the Boltzmann constant.

The positive sign of θ_{cw} indicates the existence of FM exchange interaction between the spins (Table 3). The obtained value is greater than T_C values, due to the existence of a short-range FM command. This behavior is related to the existence of a magnetic inhomogeneity [50].

On the other hand, the theoretical effective PM moments $\mu_{\text{eff}}^{\text{Theo}}$ were determined using the relation:

$$\mu_{\text{eff}}^{\text{theo}} = \sqrt{0.67\,\mu_{\text{eff}}^2\left(\text{Mn}^{3+}\right) + (0.33 - x)\,\mu_{\text{eff}}^2\left(\text{Mn}^{4+}\right)}, \tag{9}$$

where $\mu_{\text{eff}}\,(\text{Mn}^{3+}) = 4.9\ \mu_B$, $\mu_{\text{eff}}\,(\text{Mn}^{4+}) = 3.87\ \mu_B$ [51] and $\mu_B = 9.27 \times 10^{-24}$ J T^{-1}.

The obtained values of $\mu_{\text{eff}}^{\text{exp}}$, calculated using Eq. (8), and $\mu_{\text{eff}}^{\text{theo}}$ are grouped in Table 3. The difference between $\mu_{\text{eff}}^{\text{exp}}$ and $\mu_{\text{eff}}^{\text{theo}}$ can be explained by the existence of FM clusters within the PM phase inducing the additional magnetic moments. In addition, it is important to note that the percentage of Mn^{3+} and Mn^{4+} ions can be verified quantitatively by the chemical titration. In addition, it is important to note that the percentage of Mn^{3+} and Mn^{4+} ions can be verified quantitatively by the chemical titration. In fact, 50 mg of our samples were

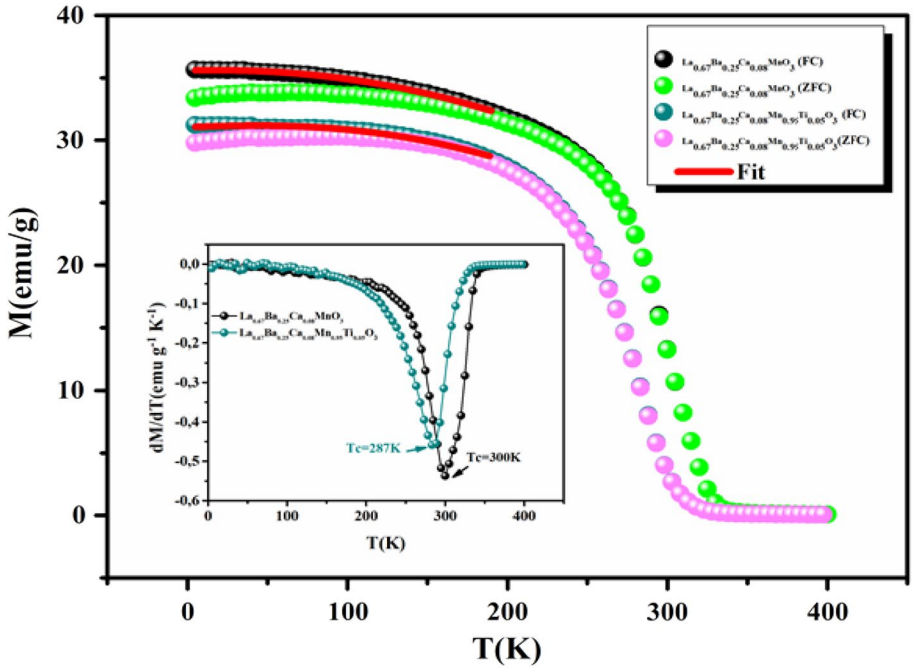

Fig. 4 Temperature dependence of the magnetization measured at magnetic field of 0.05 T for our samples. The plot of d*M*/d*T* versus *T* is depicted in the inset

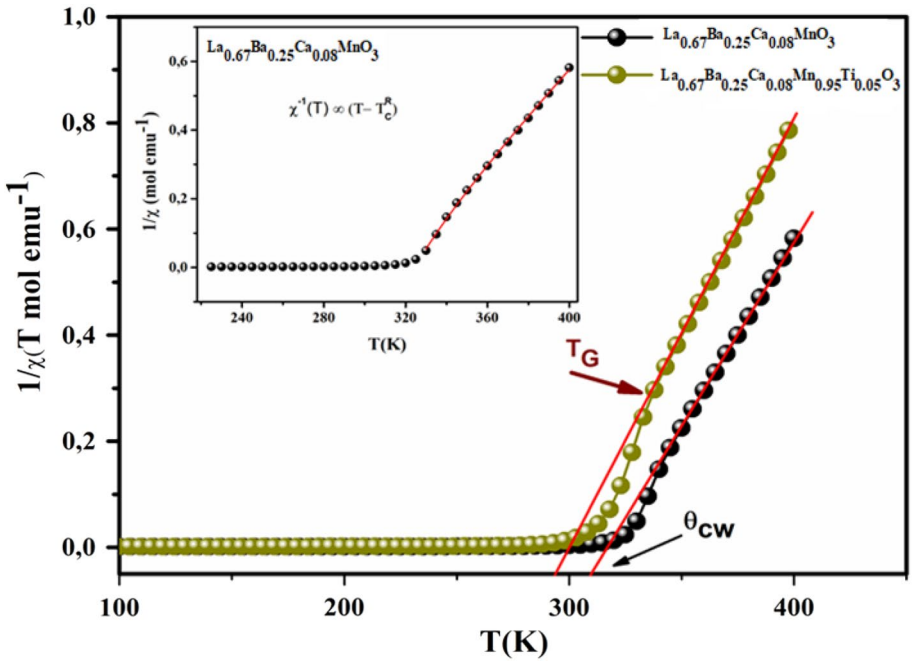

Fig. 5 Variation of the inverse susceptibility as a function of temperature for our samples. The inset shows the fit of the curve, at PM region, using Eq. 10 for $La_{0.67}Ba_{0.25}Ca_{0.08}MnO_3$ sample, as an example

dissolved in 11.2 ml of concentrated sulfuric acid and 100 mg of oxalic acid dihydrate. The obtained solution is titrated by potassium permanganate. During this titration, the following reactions occur: $C_2O_4^{2-} + 2Mn^{3+} \rightarrow 2CO_2 + 2Mn^{2+}$ and $C_2O_4^{2-} + 2Mn^{3+} \rightarrow 2CO_2 + 2Mn^{2+}$. Knowing that, $n{C_2O_4}^{2-}$ reacts $= n({C_2O_4}^{2-})_{initial} - n({C_2O_4}^{2-})_{excess}$, with $n({C_2O_4}^{2-})_{excess} = \frac{5}{2}(MnO_4^-)$. Thus, the number of moles of ${C_2O_4}^{2-}$ reacting with manganite is $2n({C_2O_4}^{2-})_{reacts} = 2n(Mn^{4+}) + n(Mn^{3+})$. Finally, by a simple calculation, the percentages of manganese, at *B*-site, are ($Mn^{3+} = 67.2\%$) and ($Mn^{4+} = 32.8\%$) for $La_{0.67}Ba_{0.25}Ca_{0.08}MnO_3$ and ($Mn^{3+} = 67.1\%$) and ($Mn^{4+} = 28.1\%$) for $La_{0.67}Ba_{0.25}Ca_{0.08}Mn_{0.95}Ti_{0.05}O_3$.

Based on the Griffiths theory [47], Griffiths phase is, generally, characterized by a magnetic susceptibility exponent (λ) of less than unity [52]. Usually, the theoretical modeling of Griffiths phase is expressed as follows [53]:

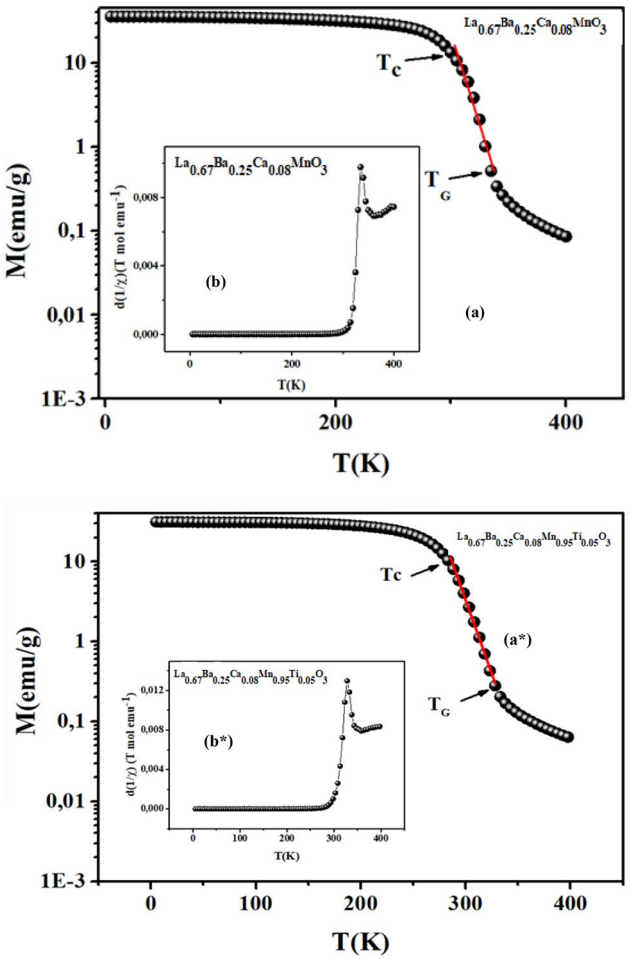

Fig. 6 (a) and (a*) show FC magnetization curves for $La_{0.67}Ba_{0.25}Ca_{0.08}MnO_3$ and $La_{0.67}Ba_{0.25}Ca_{0.08}Mn_{0.95}Ti_{0.05}O_3$ samples, respectively. The insets (b) and (b*) show $(d(1/\chi)/dT)$ as a function of temperature for our samples

Table 3 Magnetic data for $La_{0.67}Ba_{0.25}Ca_{0.08}MnO_3$ and $La_{0.67}Ba_{0.25}Ca_{0.08}Mn_{0.95}Ti_{0.05}O_3$ samples

Samples	$La_{0.67}Ba_{0.25}Ca_{0.08}MnO_3$	$La_{0.67}Ba_{0.25}Ca_{0.08}Mn_{0.95}Ti_{0.05}O_3$
T_C (K)	300	287
θ_{cw}(K)	317	303
$\mu_{eff}^{exp}(\mu_B)$	4.84	4.55
$\mu_{eff}^{Theo}(\mu_B)$	4.58	4.50
T_G (K)	335	328
T_C^R (K)	325	315
α	0.01	0.02
λ	0.13	0.22
GP (%)	11.67	15.49

$$\chi^{-1} \propto \left(T - T_C^R\right)^{1-\lambda}, \tag{10}$$

where $0 \leq \lambda \leq 1$ is the exponent describing the strength of Griffiths phase and T_C^R is the critical temperature of the random FM behavior. The choice of T_C^R was fixed using Jiang et al. method [54]. The corresponding accuracy in the estimate for T_C^R using this criterion is 1 K [52]. The exponent λ is calculated by fitting the curve presented in the inset of Fig. 5, using Eq. 10, for $La_{0.67}Ba_{0.25}Ca_{0.08}MnO_3$ as an example. Then, in the pure PM region, λ is expected to be zero.

Galitski et al. reported the effect of disorder to Griffiths phase [54]. According to them, $M(H, T)$ in Griffiths phase follow this relation:

$$M(H,T) \propto \exp\left(-\alpha \frac{T}{H}\right) \tag{11}$$

where α is a constant proportional to the total moment of magnetic cluster. We have fitted $M(T)$ curves in Griffiths phase's region shown in Fig. 6 based on Eq. 11. This formula justifies the existence of Griffiths phase and exhibits the significant role of disorder in the formation of Griffiths phase. The determined values of λ and T_C^R for our compounds are given in Table 3. The values of α and λ increase, with increasing x content. Then, the size of the magnetic cluster increases.

To get insight into the magnetic properties of our samples at low temperature, we investigated the hysteresis cycles M $(\mu_0 H)$. Figure 7 shows M $(\mu_0 H)$ at 10 K in the range of $\mu_0 H = \pm 6$ T, for $La_{0.67}Ba_{0.25}Ca_{0.08}MnO_3$ and $La_{0.67}Ba_{0.25}Ca_{0.08}Mn_{0.95}Ti_{0.05}O_3$ samples. From Fig. 7, we can see a similar behavior with a small hysteresis loop. The insets of Fig. 7 display a zoom portion of the low magnetic field region. We can remark that magnetization increased sharply at a low applied magnetic field. We observed a sharp saturation whose M_S values are 83.63 and 75.64 emu/g for $La_{0.67}Ba_{0.25}Ca_{0.08}MnO_3$ and $La_{0.67}Ba_{0.25}Ca_{0.08}Mn_{0.95}Ti_{0.05}O_3$, respectively. This indicates the typical FM behavior. Additionally, we remarked that our samples have slight values of the coercive fields $(\mu_0 H_C)$ and the remnant magnetizations (M_r). $\mu_0 H_C$ values were found to be 24.10^{-4} and 33.10^{-4} T, for $La_{0.67}Ba_{0.25}Ca_{0.08}MnO_3$ and $La_{0.67}Ba_{0.25}Ca_{0.08}Mn_{0.95}Ti_{0.05}O_3$, respectively. M_r values were found to be 1.91 and 2.77 emu/g, for $La_{0.67}Ba_{0.25}Ca_{0.08}MnO_3$ and $La_{0.67}Ba_{0.25}Ca_{0.08}Mn_{0.95}Ti_{0.05}O_3$, respectively. Here, we can conclude that our samples have a soft FM behavior. These results make them good candidates for some technological applications.

In addition to hysteresis loop, we measured magnetization as a function of the magnetic field $[M(\mu_0 H)]$ around their T_C. Figure 8a, a* show $[M(\mu_0 H)]$ around T_C, for $La_{0.67}Ba_{0.25}Ca_{0.08}MnO_3$ and

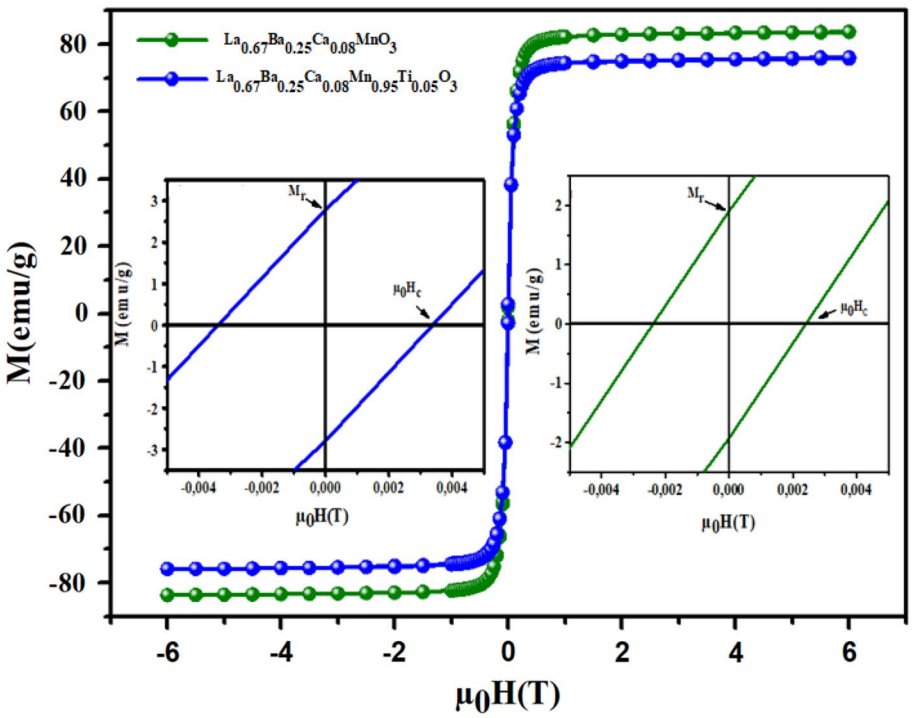

Fig. 7 Magnetic hysteresis cycles at $T = 10$ K of $La_{0.67}Ba_{0.25}Ca_{0.08}MnO_3$ and $La_{0.67}Ba_{0.25}Ca_{0.08}Mn_{0.95}Ti_{0.05}O_3$ samples. The insets show a zoom of the central portion of the hysteresis at a low field

$La_{0.67}Ba_{0.25}Ca_{0.08}Mn_{0.95}Ti_{0.05}O_3$ samples, respectively. At the low temperature region, we can see a rapid increase in magnetization at the weak magnetic field region up to 1 T. Then, M ($\mu_0 H$) curves reached saturation as a result of increasing the applied magnetic field. This indicates a typical FM behavior, which is caused by the complete alignment of the spins in our samples. To check the existence of Griffiths type phase in the compounds in the form of FM cluster system within a PM matrix, the curves of the Arrott diagram, are depicted in the inset (b) and (b*) of Fig. 8 at temperatures above and below T_C, for $La_{0.67}Ba_{0.25}Ca_{0.08}MnO_3$ and $La_{0.67}Ba_{0.25}Ca_{0.08}Mn_{0.95}Ti_{0.05}O_3$ samples, respectively. We notice that the intercepts are negative when $T > T_C$ at different temperatures, designating the absence of spontaneous magnetization and the appearance of FM clusters occurring in this temperature region [51]. Generally, the high magnetic field suppresses Griffiths phase effect which, due to the polarization of spins outside the cluster or, in another way, the FM signal, is masked by increasing PM signal as already proposed by Pramanik et al. [55].

To determine the nature of the magnetic phase transition (first or second order) for our studied samples, we used the Arrott curves ($\mu_0 H/M$ vs. M^2) using $M(\mu_0 H)$ data (Insets (c) and (c*) of Fig. 8 at temperatures, around T_C, for $La_{0.67}Ba_{0.25}Ca_{0.08}MnO_3$ and $La_{0.67}Ba_{0.25}Ca_{0.08}Mn_{0.95}Ti_{0.05}O_3$ samples, respectively) According to Banerjee's criterion [56], our samples show a positive slope, which indicates the second order phase transition.

3.3 Magnetocaloric properties

The MCE is very important for cooling technology. MCE is the heating or cooling power of a magnetic material following the application of an external magnetic field. Based on classical thermodynamic theory, the magnetic entropy change ($-\Delta S_M$) can be calculated using Maxwell's equation [57]:

$$\Delta S_M(T, \mu_0 H) = S_M(T, \mu_0 H) - S_M(T, 0) = \int_0^{\mu_0 H_{Max}} \left(\frac{\delta M(T, \mu_0)}{\delta T}\right)_{\mu_0 H} \mathrm{d}(\mu_0 H). \quad (12)$$

In the case of discrete variation of applied fields and temperature intervals, Eq. 11 can be approached as:

$$|\Delta S_M| = \sum_i \frac{M_{i+1} - M_i}{T_{i+1} - T_i} \Delta H, \quad (13)$$

where M_{i+1} and M_i are the experimental values of magnetization, obtained at the temperatures T_{i+1} and T_i, respectively.

$-\Delta S_M$ curves, under different $\mu_0 H$, are shown in Fig. 9a, a* for $La_{0.67}Ba_{0.25}Ca_{0.08}MnO_3$ and $La_{0.67}Ba_{0.25}Ca_{0.08}Mn_{0.95}Ti_{0.05}O_3$ samples, respectively.

The positive sign of $-\Delta S_M$ means that heat is released when the magnetic field is applied adiabatically. This confirms the FM character of our samples. As expected, all samples exhibited a maximum value $-\Delta S_M^{max}$ near T_C. One can observe also that $-\Delta S_M^{max}$ increases with increasing $\mu_0 H$.

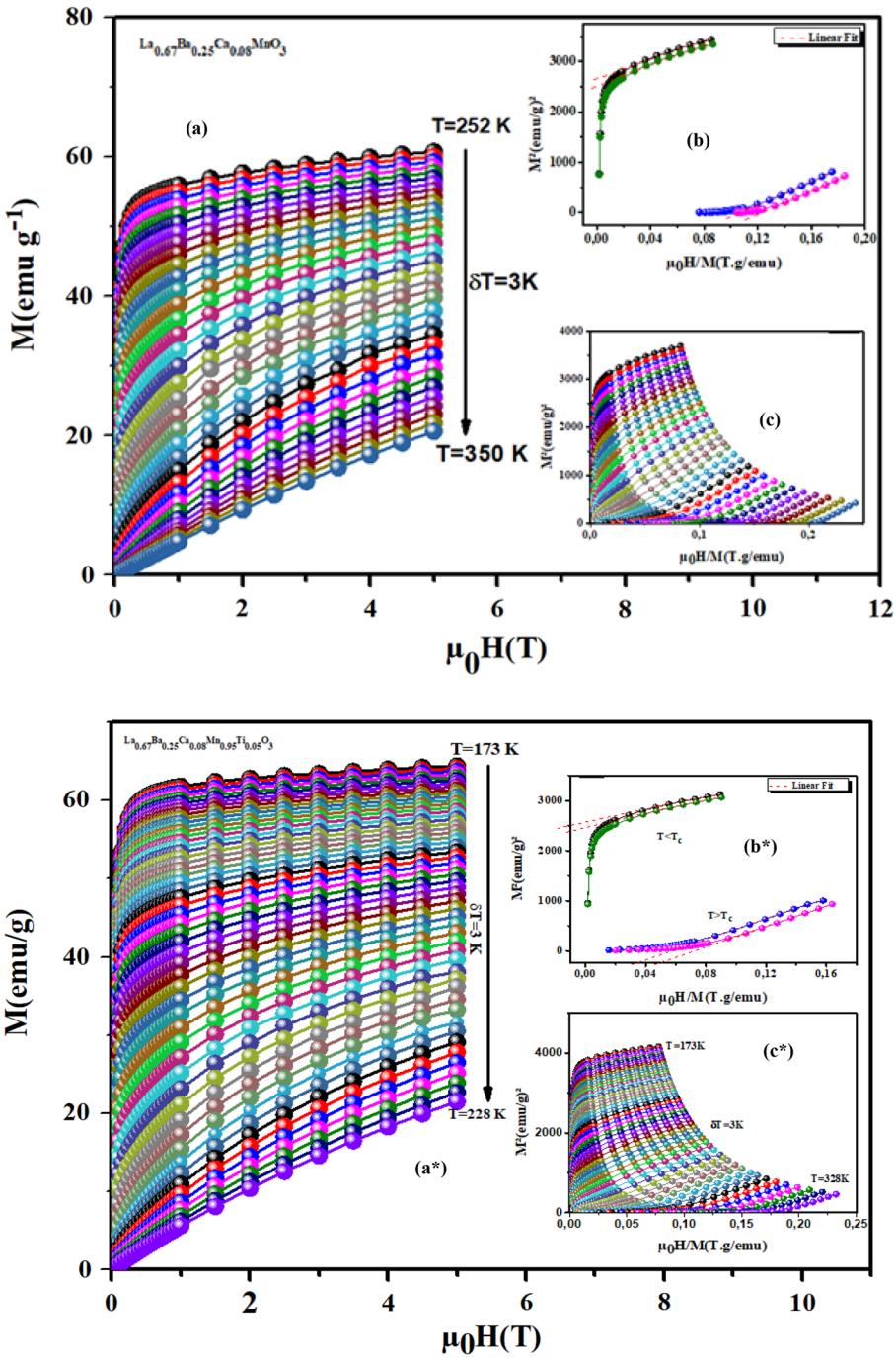

Fig. 8 (a) and (a*) show the magnetic isotherms measured at different temperatures for $La_{0.67}Ba_{0.25}Ca_{0.08}MnO_3$ and $La_{0.67}Ba_{0.25}Ca_{0.08}Mn_{0.95}Ti_{0.05}O_3$ samples, around their T_C. The insets (c) and (c*) shows M^2 vs. $(\mu_0 H)/M$. The insets (b) and (b*) shows parts of $(\mu_0 H)/M$ vs. M^2 at different temperatures above and below Tc

For $La_{0.67}Ba_{0.25}Ca_{0.08}MnO_3$ sample, $-\Delta S_M^{max}$ was found to be 3.21 J/kg. K at 5 T.

To quantify the efficiency of MC material, another very important parameter to be determined is the relative cooling power (RCP). It defines how much heat can be transferred between cold and hot sinks in one ideal refrigeration cycle. This parameter related to the maximum value of $-\Delta S_M^{max}$ and the full width at half maximum (δT_{FWHM}) can be calculated using the relation:

$$RCP = \left|\Delta S_M^{max}\right| \times \delta T_{FWHM} \quad (14)$$

The calculated values of RCP were found to be 168 and 187 J/kg at 5 T, for $La_{0.67}Ba_{0.25}Ca_{0.08}MnO_3$ and $La_{0.67}Ba_{0.25}Ca_{0.08}Mn_{0.95}Ti_{0.05}O_3$, respectively. To better understand the applicability of our compound in MR effect, the maximum values of (ΔS_M^{max}) and the RCP values are compared to other samples [58–63] (Table 4). We can deduce that our samples can be a good candidate for the magnetic refrigeration.

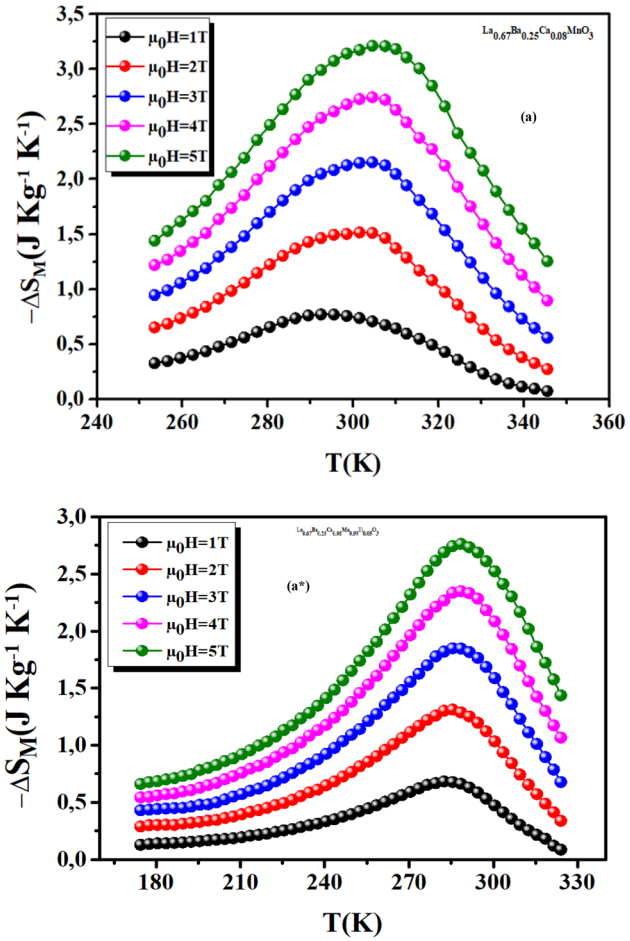

Fig. 9 (a) and (a*) show the magnetic entropy change versus temperature for $La_{0.67}Ba_{0.25}Ca_{0.08}MnO_3$ and $La_{0.67}Ba_{0.25}Ca_{0.08}Mn_{0.95}Ti_{0.05}O_3$ samples, respectively, under several magnetic applied field changes

Besides, the variation of specific heat (ΔC_P) can be determined using $-\Delta S_M$ curves, related to the magnetic field variation from 0 to $\mu_0 H$. It is expressed by the following formula [64]:

$$\Delta C_P = C_P(T, \mu_0 H) - C_P(T, 0) = T\frac{\delta \Delta S_M}{\delta T}. \quad (15)$$

The ΔC_P versus temperature under different $\mu_0 H$ is presented in Fig. 10a, a* for $La_{0.67}Ba_{0.25}Ca_{0.08}MnO_3$ and $La_{0.67}Ba_{0.25}Ca_{0.08}Mn_{0.95}Ti_{0.05}O_3$ samples, respectively. We can see that the value of ΔC_P changes abruptly from negative to positive in the vicinity of T_C. For $T > T_C$, ΔC_P is positive. It changed sign with decreasing the temperature. The sum of the two parts is the magnetic contribution to the total ΔC_P. This affects the cooling or heating power of a magnetic refrigerator [65], which confirms that ΔC_P data of a magnetic material is useful in the design of a refrigerator.

To improve MCE study of our samples, we can also calculate the adiabatic temperature change (ΔT_{ad}). It represents the temperature change of the material when adiabatically magnetized/demagnetized. It is defined as [66]:

$$\Delta T_{ad} = -\Delta S_M \frac{T}{C_{P,H}}. \quad (16)$$

ΔC_P is taken as the sum of the lattice and magnetic contributions [67, 68]:

$$C_{P,H} = C_D + C_M \text{ with } C_D = 9\,\text{KN}\left(\frac{T}{\theta_D}\right)^3 \int_0^{\theta_D} \frac{e^x x^4}{(e^x - 1)^2}\,dx \quad (17)$$

and

$$C_M = -H_{ext}\frac{\delta M}{\delta T} - \frac{1}{2}N_{int}\frac{\delta M^2}{\delta T}, \quad (18)$$

where K is the Boltzmann constant, N is the number of atoms per unit mass, θ_D is the Debye temperature. $N_{int} = \frac{3KT_C}{N_S g^2 \mu_B^2 J(J+1)}$ is the mean field constant, N_s is the number of spins per unit mass, g is the Landé factor and J is the total angular momentum. Figure 11a, a* show ΔT_{ad} as a function of temperature, under several magnetic fields, for $La_{0.67}Ba_{0.25}Ca_{0.08}MnO_3$ and $La_{0.67}Ba_{0.25}Ca_{0.08}Mn_{0.95}Ti_{0.05}O_3$ samples, respectively. We can observe that ΔT_{ad} almost conserves the same behavior of ΔS_M [69]. This confirms the FM–PM behavior in our samples.

To further study MCE, another method namely Landau's theory was suggested by Amaral et al. [70]. This theory

Table 4 Summary of magnetocaloric properties of $La_{0.67}Ba_{0.25}Ca_{0.08}MnO_3$ and $La_{0.67}Ba_{0.25}Ca_{0.08}Mn_{0.95}Ti_{0.05}O_3$ samples compared with other magnetic materials at $\mu_0 H = 5T$ for example

Samples	T_C (K)	$-\Delta S_M$ (J/kg K)	RCP (J/kg)	References
Gd	293	9.5	410	[58, 59]
$Gd_5Si_2Ge_2$	275	18.5	535	[58, 59]
$La_{0.35}Pr_{0.275}Ca_{0.375}MnO_3$	210	4.5	37.2	[60]
$La_{0.67}Ba_{0.22}Sr_{0.11}Mn_{0.9}Ti_{0.1}O_3$	289	1.33	255	[61]
$La_{0.67}Ba_{0.33}MnO_3$	292	1.48	161	[62]
$La_{0.67}Ba_{0.25}Ca_{0.08}MnO_3$	300	3.21	168	Our work
$La_{0.67}Ba_{0.25}Ca_{0.08}Mn_{0.95}Ti_{0.05}O_3$	287	2.76	187	Our work
$La_{0.67}Ba_{0.33}Mn_{0.98}Ti_{0.02}O_3$	314	3.24	307	[63]

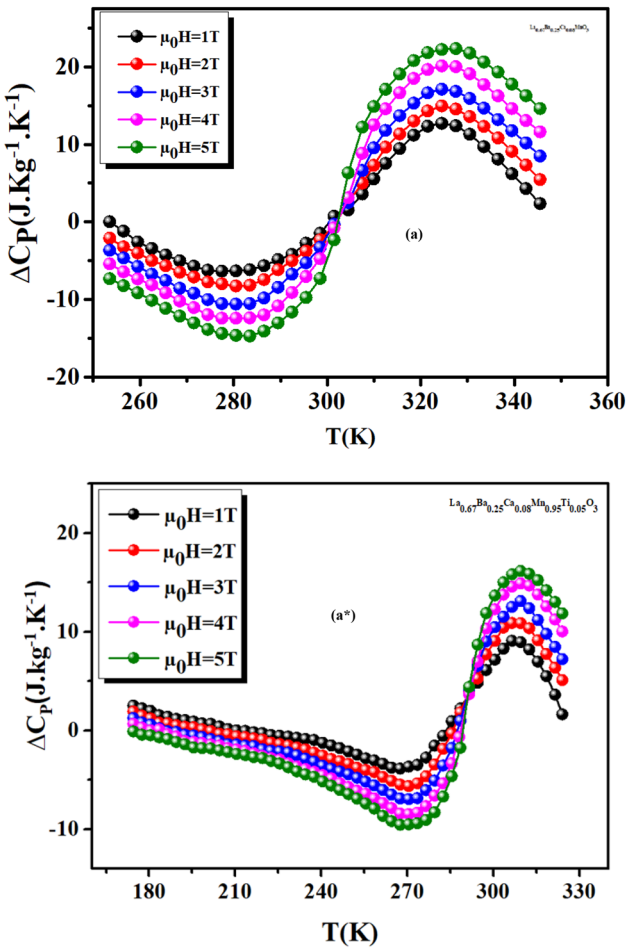

Fig. 10 (a) and (a*) show ΔC_P as function of temperature under different magnetic fields, for $La_{0.67}Ba_{0.25}Ca_{0.08}MnO_3$ and $La_{0.67}Ba_{0.25}Ca_{0.08}Mn_{0.95}Ti_{0.05}O_3$ samples, respectively

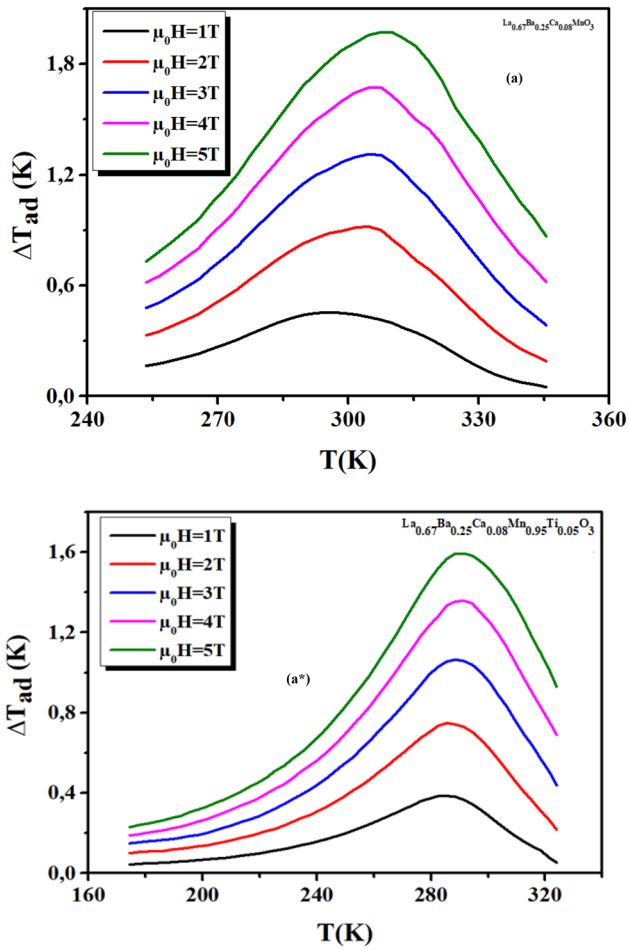

Fig. 11 (a) and (a*) show ΔT_{ad} as a function of temperature under different magnetic fields, for $La_{0.67}Ba_{0.25}Ca_{0.08}MnO_3$ and $La_{0.67}Ba_{0.25}Ca_{0.08}Mn_{0.95}Ti_{0.05}O_3$ samples, respectively

founded on the $-\Delta S_M$ data, takes into consideration the electron interaction and magnetoelastic coupling effects.

According to this theory, the variation of the Gibbs's free energy (G) can be defined as follows [71]:

$$G(T,M) = G_0 + \frac{1}{2}A(T)M^2 + \frac{1}{4}B(T)M^4 + \frac{1}{6}C(T)M^6 - \mu_0 HM. \tag{19}$$

Here $A(T)$, $B(T)$ and $C(T)$ are the Landau parameters.

From the equilibrium condition:$\frac{\partial G}{\partial M} = 0$, the magnetic equation is evaluated:

$$\frac{\mu_0 H}{M} = A(T) + B(T)M^2 + C(T)M^4. \tag{20}$$

The value of these parameters can be determined using the fit of the isothermal magnetization curve. The insets of Fig. 12a, a* present the temperature dependence of the Landau parameters for our samples.

The insets of Fig. 12a, a* show that $A(T)$ presents a minimum at T_C and $B(T)$ is positive, which presents a second-order phase transition. Consequently, this result is uniform with the previous study of the universal curve.

The corresponding $-\Delta S_M(T)$ is theoretically given by the differentiation of free energy as follows [72]:

$$\begin{aligned}\Delta S_M(T,\mu_0 H) &= -\left(\frac{\delta G}{\delta T}\right)\mu_0 H \\ &= -\frac{1}{2}A'(T)M^2 - \frac{1}{4}B'(T)M^4 - \frac{1}{6}C'(T)M^6,\end{aligned} \tag{21}$$

where $A'(T)$, $B'(T)$ and $C'(T)$ are the temperature derivatives of Landau's parameters. Figure 12a, a* present $-\Delta S_M(T)$ in comparison with the experimental data under $\mu_0 H = 5$ T, for $La_{0.67}Ba_{0.25}Ca_{0.08}MnO_3$ and $La_{0.67}Ba_{0.25}Ca_{0.08}Mn_{0.95}Ti_{0.05}O_3$ samples, respectively. A good agreement is found between these two curves, near T_C. These results indicate that

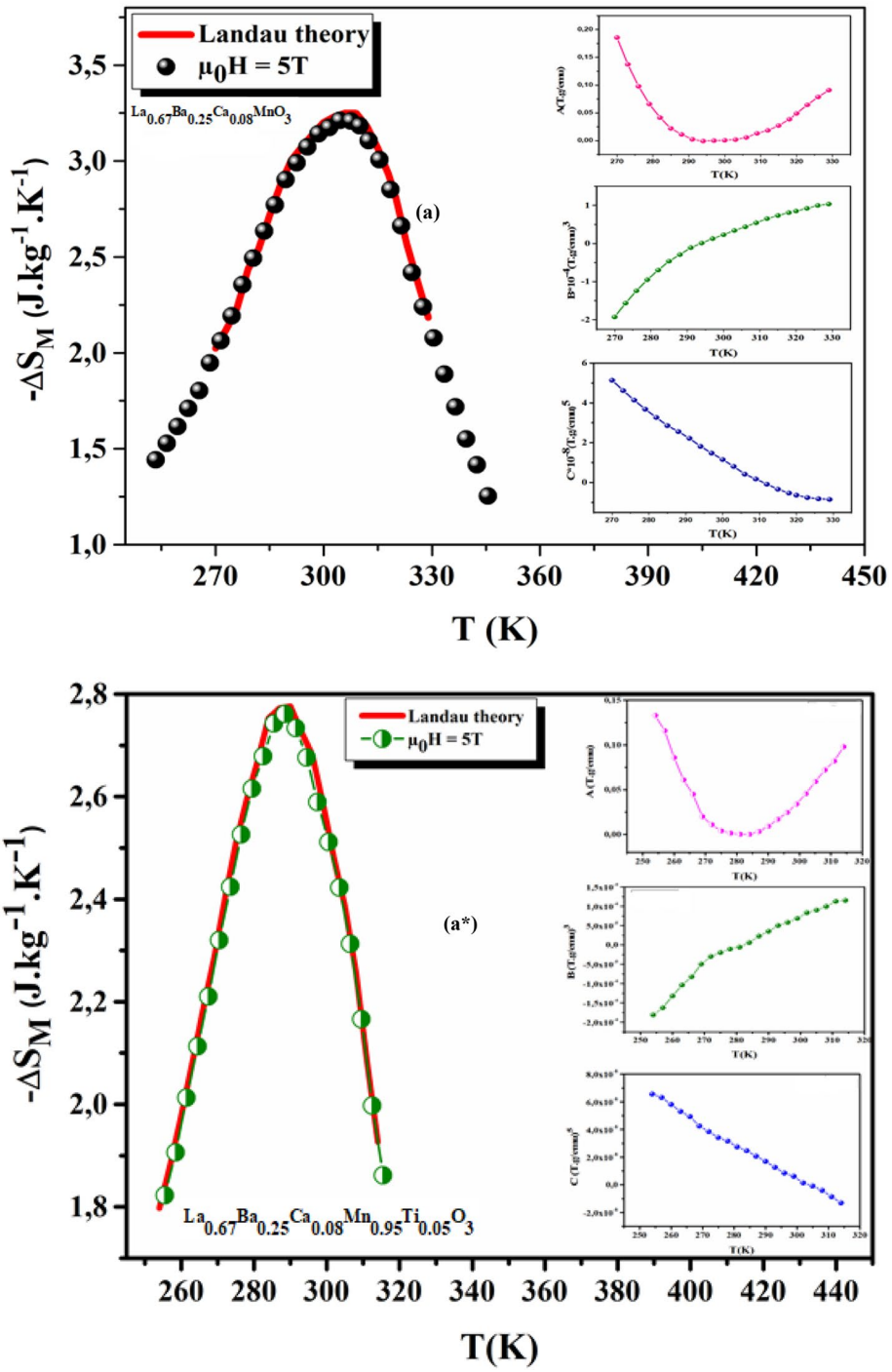

Fig. 12 (a) and (a*) show the variations of experimental (red diamond) and calculated magnetic entropy change versus temperature under 5 T for $La_{0.67}Ba_{0.25}Ca_{0.08}MnO_3$ and $La_{0.67}Ba_{0.25}Ca_{0.08}Mn_{0.95}Ti_{0.05}O_3$ samples, respectively. The insets show the Landau's coefficients $A(T)$, $B(T)$ and $C(T)$

magnetoelastic coupling and electronic interaction may explain the MCE properties of these compounds [73].

To understand the influence of the magnetic fields on $-\Delta S_M(T)$, Oesterreicher et al. [74] proposed the relation between them, which can be expressed as:

$$-\Delta S_M = a(\mu_0 H)^n. \tag{22}$$

Here 'a' is a constant and the exponent n depends on the magnetic field and temperature. It can be locally calculated as:

$$n = \frac{d \ln \Delta S_M}{d \ln \mu_0 H}. \tag{23}$$

The value of n is determined from the linear plot of $\ln(-\Delta S_M)$ versus $\ln(\mu_0 H)$ using Eq. 22 (Fig. 13). One can see that the value of n obtained at T_C is equal to 0.690 and 0.677, for $La_{0.67}Ba_{0.25}Ca_{0.08}MnO_3$ and $La_{0.67}Ba_{0.25}Ca_{0.08}Mn_{0.95}Ti_{0.05}O_3$, respectively.

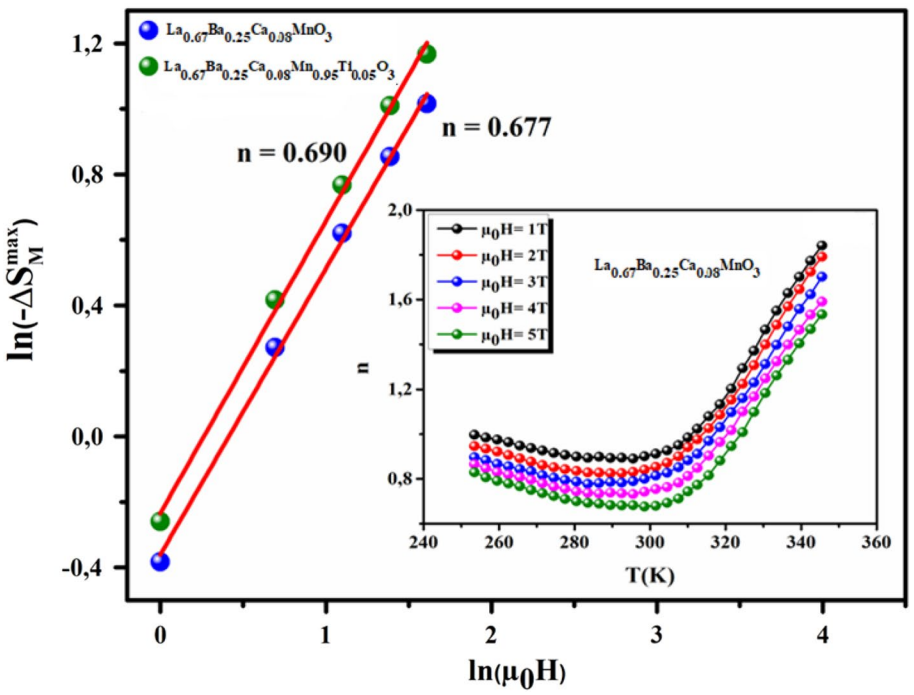

Fig. 13 Field dependence of $-\Delta S_M^{\max}$ (inset represents magnetic field dependence of local exponent n measured at different fields for $La_{0.67}Ba_{0.25}Ca_{0.08}MnO_3$ sample, as an example

Based on the mean field approach, the field dependence of $-\Delta S_M$ corresponds to $n = 2/3$ at T_C. This parameter value (n) was estimated to be about 1 and 2 below and above the transition temperature, respectively.

The inset of Fig. 13 presents the temperature dependence of the exponent n, for $La_{0.67}Ba_{0.25}Ca_{0.08}MnO_3$ as an example. n exhibits a moderate decrease with increasing temperature, with a minimum value in the vicinity of T_C, sharply increasing above T_C. These values are very close to the values of mean field model. This can be due to the existence of local inhomogeneity [75, 76]. The results were comparable to those found by other authors [77, 78].

Moreover, to confirm the nature of the phase transition in our samples, Franco et al. [79] have proposed a phenomenological universal curve. This method was carried out by normalizing

$-\Delta S_M$ by their respective maximum $-\Delta S_M^{\max}$, namely $\Delta S' = \Delta S_M(T)/\Delta S_M^{\max}$ and rescaling the temperature axis using two other reference temperatures in a different way below and above T_C. The positions of these additional reference temperatures in the curve correspond to: $\theta = \pm 1$:

$$\theta = \begin{cases} -(T - T_C)/(T_{r1} - T_C) & T \le T_C \\ (T - T_C)/(T_{r2} - T_C) & T > T_C \end{cases}, \quad (24)$$

where T_{r1} and T_{r2} are two reference temperatures which have been selected as those corresponding to $\Delta S_M(T_{r1,2}) = \Delta S_M^{\max}/2$.

According to $T_{r1}$and T_{r2}, the rescaled $-\Delta S_M(T)$ curves measured with different applied magnetic fields will collapse into a single curve only for second-order phase transition. However, for materials with a first-order phase transition, the rescaled $\Delta S_M(T)$ curves did not follow a universal behavior.

Figure 14a, a* show the universal curve for $La_{0.67}Ba_{0.25}Ca_{0.08}MnO_3$ and $La_{0.67}Ba_{0.25}Ca_{0.08}Mn_{0.95}Ti_{0.05}O_3$, respectively. It is clear that all curves collapse on a single universal curve. This proves that the transition is of a second order. The obtained results are in good agreement with the analysis of Banerjee's criterion.

4 Conclusion

To sum up, we prepared $La_{0.67}Ba_{0.25}Ca_{0.08}MnO_3$ and $La_{0.67}Ba_{0.25}Ca_{0.08}Mn_{0.95}Ti_{0.05}O_3$, using the Flux method and then studied its structural, magnetic and magnetocaloric properties. Rietveld refinement of X-ray diffraction patterns demonstrates that our samples crystallize in a rhombohedral structure with $R\bar{3}c$ space group. These samples exhibit a second-order ferromagnetic–paramagnetic phase transition. In the paramagnetic region, a non-linear behavior, for our samples, is observed in χ^{-1} vs. T curves. This can be explained by the existence of Griffiths phase. Around room temperature, our samples have an important $-\Delta S_M$ (3.21 J/kg and 2.76 J/kg at 5 T, for $La_{0.67}Ba_{0.25}Ca_{0.08}MnO_3$ and $La_{0.67}Ba_{0.25}Ca_{0.08}Mn_{0.95}Ti_{0.05}O_3$, respectively). The field dependence of $-\Delta S_M$ is also analyzed,

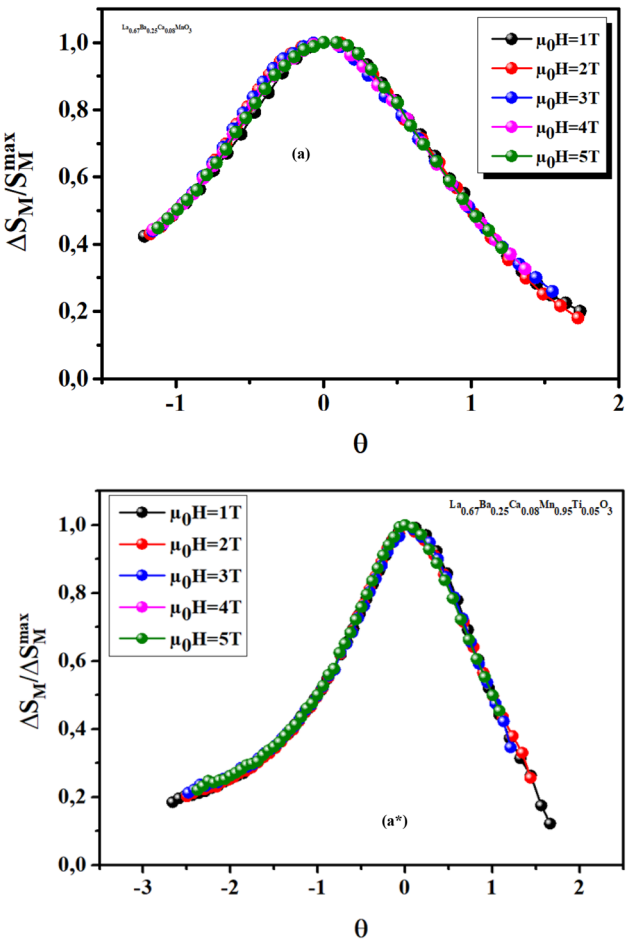

Fig. 14 (a) and (a*) show the normalized entropy change versus rescaled temperature (θ) for different applied magnetic fields for $La_{0.67}Ba_{0.25}Ca_{0.08}MnO_3$ and $La_{0.67}Ba_{0.25}Ca_{0.08}Mn_{0.95}Ti_{0.05}O_3$ samples, respectively

showing the power law dependence, $-\Delta S_M = a(\mu_0 H)^n$, where $n = 0.690$ and 0.677, for $La_{0.67}Ba_{0.25}Ca_{0.08}MnO_3$ and $La_{0.67}Ba_{0.25}Ca_{0.08}Mn_{0.95}Ti_{0.05}O_3$, respectively at their T_C. Additionally, we determined the RCP value. It was found to be 168 and 187 J/kg for $La_{0.67}Ba_{0.25}Ca_{0.08}MnO_3$ and $La_{0.67}Ba_{0.25}Ca_{0.08}Mn_{0.95}Ti_{0.05}O_3$, respectively. According to the universal curve for the temperature dependence of $-\Delta S_M$ measured for different maximum fields, paramagnetic–ferromagnetic phase transition observed for our samples were of second-order. From the hysteresis cycles, at 10 K for the studied samples, we can note a typical soft ferromagnetic behavior with a low hysteresis loop and coercive field. These confirm that the magnetic domains can rotate easily to the direction of the magnetic field. All results indicate that our samples could be a potential candidate for magnetic refrigeration.

References

1. Ah Dhahri, E. Dhahri, E.K. Hlil, RSC Adv. **9**, 5530 (2019)
2. K. Cherif, A. Belkahla, J. Dhahri, J. Alloys Compd. **777**, 358 (2019)
3. M.A. Gdaiem, Ah Dhahri, J. Dhahri, E.K. Hlil, RSC Adv. **7**, 10928 (2017)
4. K. Gupta, P.T. Das, T.K. Nath, P.C. Jana, A.K. Meikap, Int. J. Soft Comput. Eng. **2**, 246 (2012)
5. M.A. Gdaiem, Ah Dhahri, J. Dhahri, E.K. Hlil, Mater. Res. Bull. **88**, 91 (2017)
6. C.R. Serrao, A. Sundaresan, C.N.R. Rao, J. Phys. Condens. Matter **19**, 496217 (2007)
7. F. Borgatti, C. Park, A. Herpers, F. Offi, R. Egoavil, Y. Yamashita, A. Yang, M. Kobata, K. Kobayashi, J. Verbeeck, G. Panaccione, R. Dittmann, Nanoscale **5**, 3954 (2013)
8. C. Reitz, P.M. Leufke, R. Schneider, H. Hahn, T. Brezesinski, Chem. Mater. **26**, 5745 (2014)
9. E. Dagotto, T. Hotta, A. Moreo, Phys. Rep. **344**, 1 (2001)
10. B. Uthaman, P. Manju, S. Thomas, D.J. Nagar, K.G. Suresh, M.V. Varma, Phys. Chem. Chem. Phys. **19**, 12282 (2017)
11. A. Turcaud, A.M. Pereira, K.G. Sandeman, Phys. Rev. B Condens. Matter **90**, 024410 (2014)
12. S.K. Misra, S.I. Andronenko, S. Asthana, D. Bahadur, J. Magn. Magn. Mater. **22**, 2902 (2010)
13. J.W. Chen, G. Narsinga Rao, Mater. Chem. Phys. **136**, 254 (2012)
14. A. Varvescu, I.G. Deac, Phys. B Condens. Matter **470–471**, 96 (2015)
15. S. Othmani, M. Balli, A. Cheikhrouhou, Solid State Commun. **192**, 51 (2014)
16. M.-H. Phana, S.-C. Yu, J. Mag, Magn. Mater. **308**, 325 (2007)
17. C.F. Pena, M.E. Soffner, A.M. Mansanares, J.A. Sampaio, F.C.G. Gandra, E.C. da Silva, H. Vargas, Phys. B Cond. Matter **523**, 39 (2017)
18. I. Betancourt, L. Lopez Maldonado, J.T. Elizalde Galindo, J. Magn. Magn. Mater. **401**, 812 (2016)
19. F. Ben Jemaa, S. Mahmood, M. Ellouze, E.K. Hlil, F. Halouani, I. Bsoul, M. Awawdeh, Solid State Sci. **37**, 121 (2014)
20. M. Abassi, N. Dhahri, J. Dhahri, E.K. Hlil, Phys. B **449**, 138 (2014)
21. N. Kumar, H. Kishan, A. Rao, V.P.S. Awana, J. Appl. Phys. **107**, 083905 (2010)
22. N.V. Dai, D.V. Son, S.C. Yu, L.V. Bau, L.V. Hong, N.X. Phuc, D.N.H. Nam, Phys. Status Solid **244**, 4570 (2007)
23. P. Nisha, S.S. Pillai, A. Darbandi, M.R. Varma, K.G. Suresh, H. Hahn, Mater. Chem. Phys. **136**, 66 (2012)
24. A. Belkahla, K. Cherif, J. Dhahri, K. Taibi, E.K. Hlil, RSC Adv. **7**, 30707 (2017)
25. H. Kawanaka, H. Bando, Y. Nishihara, J. Korean Phys. Soc. **63**, 529 (2013)
26. J. Liu, M. Hou, J. Yi, S. Guo, C. Wang, Y. Xia, Energy Environ. Sci. **7**, 705 (2014)
27. W. ZhenYao, L. Biao, M. Jin, X. DingGuo, Electrochim. Acta **117**, 285 (2014)
28. H.M. Rietveld, J. Appl. Cryst. **2**, 65 (1969)
29. T. Roisnel, J. Rodriguez-Carvajal, Computer Program FULLPROF, LLB-LCSIM (2003)
30. S.E. Kossi, S. Ghodhbane, S. Mnefgui, J. Dhahri, E.K. Hlil, J. Magn. Magn. Mater. **395**, 134 (2015)
31. Shao-ying Zhang, Peng Zhao, Zhao-hua Cheng, Run-wei Li, Ji-rong Sun, Hong-wei Zhang, Bao-gen Shen, Phys. Rev. B **64**, 212404 (2001)
32. B. Vertruyen, S. Hébert, A. Maignan, C. Martin, M. Hervieu, B. Raveau, J. Magn. Magn. Mater. **280**, 75 (2004)

33. V.M. Goldschmidt, *Geochemistry* (Oxford University Press, Oxford, 1958), p. 730
34. R.D. Shannon, C.T. Prewitt, Acta Cryst. B **25**, 925 (1969)
35. A.K. Zak, W.H. Abd Majid, M.E. Abrishami, R. Yousefi, Solid State Sci. **13**, 251 (2011)
36. H.E. Sekrafi, A.B.J. Kharrat, M.A. Wederni, N. Chniba-Boudjada, K. Khirouni, W. Boujelben, J. Mater. Sci. Mater. Electron. **30**, 876 (2019)
37. G.K. Williamson, W.H. Hall, Acta Metall. **1**, 22 (1953)
38. K.S. Rao, B. Tilak, KChV Rajulu, A. Swathi, H. Workineh, J. Alloys Compd. **509**, 7121 (2011)
39. M.H. Ehsani, T. Raoufi, F.S. Razavib, J. Magn. Magn. Mater. **475**, 484–492 (2019)
40. Ah Dhahri, E. Dhahri, E.K. Hlil, J. Alloys Compd. **727**, 449 (2017)
41. K. Cherif, A. BenKahla, J. Dhahri, E.K. Hlil, Ceram. Int. **42**, 10537 (2016)
42. E. Rodriguez, I. Alvarez, M.L. Lopez, M.L. Veiga, C. Pico, J. Solid State Chem. **148**, 479 (1999)
43. P.G. Radaelli, G. Iannone, M. Marezio, H.Y. Hwang, S.W. Cheong, J.D. Jorgensen, D.N. Argyriou, Phys. Rev. B **56**, 8265 (1997)
44. M.A. Zaidi, J. Dhahri, I. Zeydi, T. Alharbi, H. Belmabrouk, RSC Adv. **7**, 43590 (2017)
45. C.N.R. Rao, *Advances in Chemistry* (Word Scientific Publishing Co. Pte. Ltd., Singapore, 1994)
46. G.G. Lonzarich, L. Taillefer, J. Phys. C Solid State Phys. **18**, 4339 (1985)
47. R.B. Griffiths, Phys. Rev. Lett. **23**, 17 (1969)
48. P. Tong, B.J. Kim, D. Kwon, T. Qian, S.I. Lee, S.W. Cheong, B.G. Kim, Phys. Rev. B **77**, 184432 (2008)
49. N. Dhahri, A. Dhahri, K. Cherif, J. Dhahri, K. Taibi, E. Dhahri, J. Alloys Compd. **496**, 69 (2010)
50. Ah Dhahri, M. Jemmali, K. Taibi, E. Dhahri, E.K. Hlil, J. Alloy. Compd. **618**, 488 (2015)
51. C. Kittel, *Introduction to Solid State Physics* (Wiley, New York, 1986), p. 118
52. W. Jiang, X.Z. Zhou, G. Williams, Y. Mukovskii, K. Glazyrin, Phys. Rev. Lett. **99**, 177203 (2007)
53. V.N. Krivoruchko, M.A. Marchenko, Y. Melikhov, J. Phys. Rev. B **82**, 064418 (2010)
54. V.M. Galitski, A. Kaminski, S.D. Sarma, Phys. Rev. Lett. **92**, 177203 (2004)
55. A.K. Pramanik, A. Benerjee, J. Phys. Rev. B **81**, 024431 (2010)
56. S.K. Banerjee, Phys. Lett. **12**, 16–17 (1964)
57. X. Bohigas, J. Tejada, M.L. Marınez-Sarrion, S. Tripp, R. Black, J. Magn. Magn. Mater **208**, 85 (2000)
58. V.K. Pecharsky, K.A. Gschneidner Jr., Phys. Rev. Lett. **78**, 4494–4497 (1997)
59. V.K. Pecharsky, K.A. Gschneidner, A.O. Tsokol, Rep. Prog. Phys. **68**, 1479–1539 (2005)
60. M.H. Phan, S. Chandra, N.S. Bingham, H. Srikanth, C.L. Zhang, H.D. Chinh et al., Appl. Phys. Lett. **97**, 242506 (2010)
61. F.B. Jemaa, S.H. Mahmood, M. Ellouze, E.K. Hlil, F. Halouani, Ceram. Int. **41**, 8191–8202 (2015)
62. D.T. Morelli, A.M. Mance, J.V. Mantese, A.L. Micheli, J. Appl. Phys. **79**, 373–375 (1996)
63. M. Oumezzine, S. Zemni, O. Pena, J. Alloys Compd. **508**, 292 (2010)
64. M.H. Phan, H.X. Peng, S.C. Yu, N.D. Tho, N. Chau, J. Magn. Magn. Matter **285**, 199 (2005)
65. A. Marzouki-Ajmi, W. Cheikhrouhou-Koubaa, M. Koubaa, A. Cheikhrouhou, J. Supercond. Novel Magn. **28**, 1065 (2014)
66. M.A. Hamad, J. Supercond. Novel Magn. **27**, 277 (2014)
67. A.H. Morrish, *The Physical Principle of Magnetism* (Wiley, New York, 1965). **(Search Pub Med)**
68. N.W. Ashcroft, N.D. Mermin, *Solid State Physics* (Saunders College Publishing, London, 1976). **(Search Pub Med)**
69. K. Riahi, I. Messaoui, A. Ezaami, F. Cugini, M. Solzi, W. Cheikhrouhou-Koubaa, A. Cheikhrouhou, Phase Transit. **91**, 691 (2018)
70. V.S. Amaral, J.S. Amaral, J. Magn. Magn. Mater. **272–276**, 2104 (2004)
71. J.S. Amaral, V.S. Amaral, J. Magn. Magn. Mater. **322**, 1552 (2010)
72. M.S. Anwar, S. Kumar, F. Ahmed, N. Arshi, G.W. Kim, B.H. Koo, J. Korean Phys. Soc. **60**, 1587 (2012)
73. J.S. Amaral, M.S. Reis, V.S. Amaral, T.M. Mendonc, J.P. Araujo, M.A. Sa, P. Btavares, J.M. Vieira, J. Magn. Magn. Mater. **686**, 290–291 (2005)
74. H. Oesterreicher, F.T. Parker, J. Appl. Phys. **55**, 4334 (1984)
75. V. Franco, J.S. Blázquez, A. Conde, Appl. Phys. Lett. **89**, 222512 (2006)
76. V. Franco, J.S. Blazquez, A. Conde, Appl. Phys. **100**, 064307 (2006)
77. V. Franco, C.F. Conde, J.S. Blazquez, A. Conde, P. Svec, D. Janičkovic, L.F. Kiss, J. Appl. Phys. **101**, 093903 (2007)
78. M. Pękala, J. Appl. Phys. **108**, 113913 (2010)
79. V. Franco, A. Conde, Int. J. Refrig. **33**, 465473 (2010)